

Few-nm tracking of current-driven magnetic vortex orbits using ultrafast Lorentz microscopy

Marcel Möller ¹, John H. Gaida ¹, Sascha Schäfer¹ & Claus Ropers¹✉

Transmission electron microscopy is one of the most powerful techniques to characterize nanoscale magnetic structures. In light of the importance of fast control schemes of magnetic states, time-resolved microscopy techniques are highly sought after in fundamental and applied research. Here, we implement time-resolved Lorentz imaging in combination with synchronous radio-frequency excitation using an ultrafast transmission electron microscope. As a model system, we examine the current-driven gyration of a vortex core in a 2 μm -sized magnetic nanoisland. We record the trajectory of the vortex core for continuous-wave excitation, achieving a localization precision of ± 2 nm with few-minute integration times. Furthermore, by tracking the core position after rapidly switching off the current, we find a transient increase of the free oscillation frequency and the orbital decay rate, both attributed to local disorder in the vortex potential.

¹4th Physical Institute-Solids and Nanostructures, University of Göttingen, Friedrich-Hund-Platz 1, 37077 Göttingen, Germany. ✉email: claus.ropers@uni-goettingen.de

Magnetism gives rise to an incredibly rich set of nanoscale phenomena, including topological textures such as skyrmions^{1–3} and vortices⁴. Dynamical control of spin structures down to sub-picosecond timescales is facilitated by a multitude of interactions involving spin-torques^{5–7} or optical excitations^{8–11}. These features have shown immediate relevance in novel applications, exemplified in (skyrmion) racetrack memory^{12,13}, magnetic random access memory¹⁴, and vortex oscillators as radiofrequency (RF) sources^{15,16} or for neuromorphic computing^{17,18}. Observing these magnetic phenomena on their intrinsic length and time scales requires experimental tools capable of simultaneous nanometer spatial and nanosecond to femtosecond temporal resolution. Whereas photoelectron¹⁹ and magneto-optical schemes using pulsed radiation sources from the visible²⁰ to the x-ray^{21–23} regime inherently offer high temporal resolution, the particular advantages of electron beam techniques have yet to be fully exploited in the ultrafast domain.

Transmission electron microscopy (TEM) facilitates quantitative magnetic imaging with very high spatial resolution approaching the atomic level using aberration-corrected instruments^{24,25} and holographic approaches^{26–29}, while also allowing for structural or chemical analysis. Importantly, the versatile in situ environment of TEM enables the observation of nanoscale magnetic changes with optical^{11,30,31} or electrical stimuli^{32–34}. Time-resolved transmission electron microscopy^{35–37} has in some instances been used to address magnetization dynamics^{38–41}. The recent advance of highly coherent photoelectron sources^{42,43} promises substantially enhanced contrast and resolution in ultrafast magnetic imaging⁴⁴, but has, to date, not been combined with synchronized electrical stimuli.

In this work, we address this problem and realize ultrafast Lorentz microscopy with in situ RF current excitation. The technique is made possible by using a transmission electron microscope with a pulsed photoelectron source. Synchronizing the electron pulses at the sample with the RF current, images of the instantaneous state of the system for a given RF phase can be acquired. The controlled variation of the phase allows for recording high-speed movies with a temporal resolution independent of the readout speed of the detector, but given by the duration of the electron pulses and the quality of the electrical synchronization.

Results

Time-resolved Lorentz microscopy. The experiments were conducted at the Göttingen ultrafast transmission electron microscope (UTEM), which features ultrashort electron pulses of high beam quality from a laser-triggered field emitter⁴². Employing a linear photoemission process, the UTEM allows for a flexible variation of the electron pulse parameters in terms of repetition rate and pulse duration^{42,45}. In the present study, we employ electron pulses at a repetition rate of 500 kHz, driven by frequency doubled optical pulses from an amplified Ti:sapphire laser with a central wavelength of 400 nm and a pulse duration of 2.2 ps.

We demonstrate the capabilities of our instrument by studying the model system of a spin-transfer torque driven vortex oscillator^{41,46–49}. The sample is a $2.1 \times 2.1 \mu\text{m}^2$ large and 26 nm thick polycrystalline permalloy ($\text{Ni}_{81}\text{Fe}_{19}$) square. Its magnetic configuration consists of four domains forming a flux closure (Landau) state with an in-plane magnetization pointing along the edges of the nanoisland and a perpendicular magnetized core with a diameter on the order of 10 nm refs. ^{4,50}. The curl c specifies whether the in-plane magnetization rotates counter-clockwise ($c = +1$) or clockwise ($c = -1$), whereas the polarity p indicates if

the core magnetization is parallel ($p = 1$) or antiparallel ($p = -1$) to the z -axis of the coordinate system defined in Fig. 1.

Two edges of the structure are electrically contacted with 100 nm thick gold electrodes (see Fig. 1) which terminate in wire-bonding pads. The sample is installed in a custom-made TEM holder that allows for in situ RF-current excitation up to the GHz-regime^{32–34}. RF-currents are generated with an arbitrary waveform generator (AWG) synchronized to the photodiode signal from the laser oscillator. This allows us to create custom waveforms, such as continuous or few-cycle sine waves, with a fixed, software-programmable timing between the probing electron pulse and the phase of the excitation. Driven by alternating currents, the vortex structure exhibits a resonance behavior, in which the core traces out an ellipsoidal trajectory^{32,49,51,52}. The trajectory of the vortex core under the simultaneous influence of spin-transfer torques and Oersted fields is predicted by a harmonic oscillator model^{51,52}.

To image the magnetic configuration of our sample, we employ Fresnel-mode Lorentz microscopy^{53,54}, a form of defocus phase contrast (see Fig. 1). In a classical picture, magnetic contrast arises from the Lorentz force: When the parallel beam of electrons passes through the magnetic field of the sample, electrons experience a momentum change perpendicular to their propagation direction and proportional to the local magnetic field. By slightly defocusing the imaging system of the microscope, this

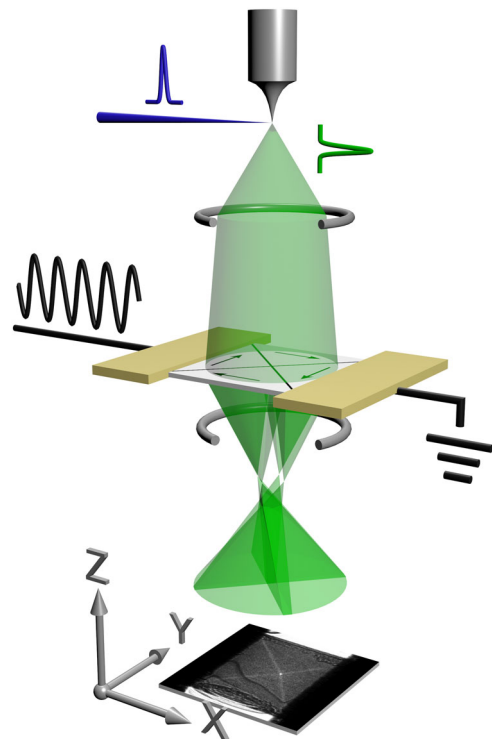


Fig. 1 Schematic representation of time-resolved Lorentz microscopy combined with synchronous radiofrequency sample excitation. An ultrashort electron pulse (green) is generated via a linear photoemission process from an optical laser pulse (blue) inside the electron gun. A magnetic sample (light gray) is stroboscopically illuminated with a near-parallel electron beam and imaged onto a transmission electron microscope camera. Employing a small defocus in the imaging conditions gives rise to magnetic contrast (exemplary image shown in the bottom). Dynamics in the sample are excited in situ with radiofrequency currents (black) phase-locked to multiples of the laser repetition rate, creating the appearance of a static image. A controlled change of the radiofrequency phase between images allows the entire dynamic process to be mapped in time.

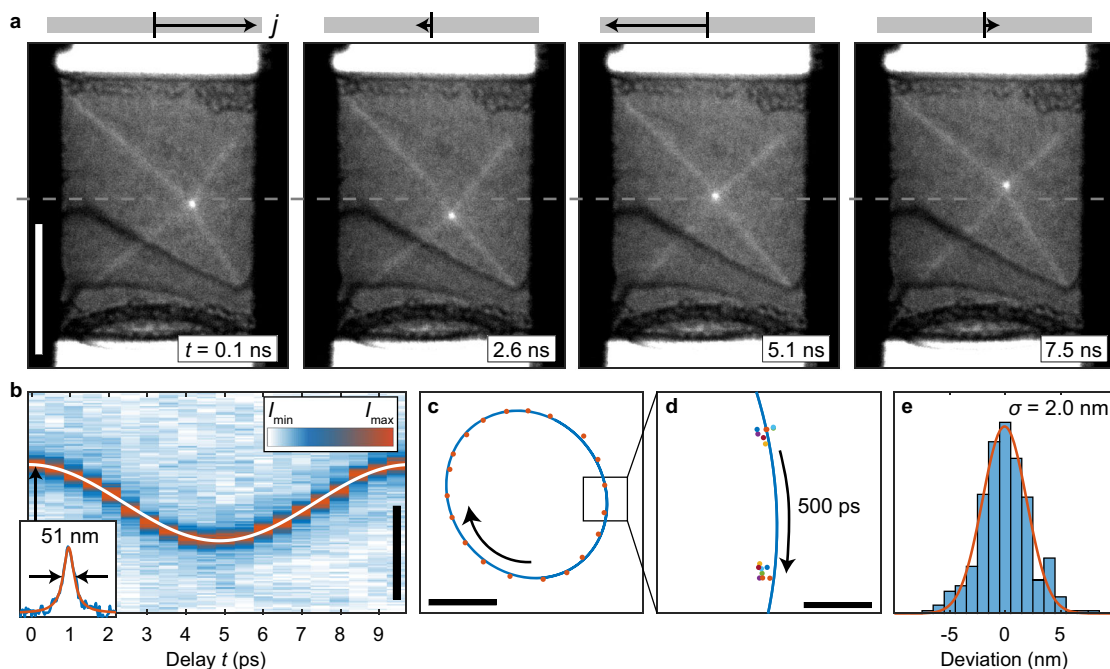


Fig. 2 Continuous-wave excitation at a frequency of $f_{\text{ex}} = 101.5 \text{ MHz}$ and a current density of $j = 1.7 \times 10^{11} \text{ A m}^{-2}$. **a** Four time-resolved Lorentz micrographs acquired in time steps of 2.5 ns at a defocus of $520 \mu\text{m}$ (scale bar: $1 \mu\text{m}$). **b** Line profiles at the position of the vortex core along the x -direction, closely resembling a sinusoidal displacement. White: Best fit of a harmonic oscillator model (scale bar: 300 nm). **(b, Inset)** Blue: Example of a single line profile at $t = 0.1 \text{ ps}$. Red: Fitted Lorentzian line shape. **c** Red: Mean vortex core position determined from set of eight identical Lorentz micrographs at each delay t . Blue: Best fit of the harmonic oscillator model (scale bar: 100 nm). **d** Example of the spatial spread of the tracked vortex position (scale bar: 20 nm). **e** Distribution of the spatial deviation from the mean for all position measurements in x - and y -direction.

transverse momentum gives rise to a contrast which scales with the magnitude of the z -component of the curl of the sample's induction^{53,54}.

A Lorentz micrograph of the sample acquired with a continuous electron beam is depicted in the bottom of Fig. 1. The X-shaped lines indicate the position of the domain walls. A peak in the contrast arises at the intersection of the domain walls, and marks the position of the vortex core. The core itself does not contribute to the magnetic contrast, as its magnetization points along the beam propagation direction. The dark lines in the lower half of the image are Bragg lines of the single-crystal silicon substrate, which locally scatter intensity out of the forward beam, and the dark areas at the lateral edges stem from the gold contacts.

Continuous excitation. In a first experiment, we excite the vortex with a continuous sinusoidal current at a frequency of $f_{\text{ex}} = 101.5 \text{ MHz}$. This frequency maximizes the orbit diameter of the gyration, as determined from a preliminary measurement using a continuous electron beam (see Methods). To resolve a whole period, we acquire images for 21 delays t at intervals of 500 ps. At every delay t , we record 32 time-resolved micrographs, each with an integration time of one minute. The delay times given are quantitative with respect to the maximum of the driving field, enabled by in situ electron beam deflection near the contacts (see Methods)³³. After applying a drift-correction, we sum over identical micrographs and obtain a movie of the vortex dynamics, which is presented in Supplementary Movie 1.

Between the four exemplary frames in Fig. 2 a, acquired at time steps of 2.5 ns, the vortex core is clearly displaced and performs a clockwise rotation, implying a polarity of $p = -1$ refs. 46,51. The curl of the vortex is $c = -1$, determined from the contrast of the domain walls (bright or dark; here: bright) and the choice of

imaging conditions (over- or underfocus; here: overfocus)⁵⁵. Line profiles along the x -direction at the position of the vortex core are displayed in Fig. 2b, following a near-sinusoidal trajectory. The inset in Fig. 2b depicts a single line profile (blue line) with a Lorentzian line-shape (red line) fitted to the data. The mean full-width-half-max (FWHM) of the the peak is $51 \pm 1 \text{ nm}$, averaged over all delays t and both spatial dimensions. It should be noted that this size does not represent the vortex core diameter—which is expected to be on the order of $10\text{--}20 \text{ nm}$ ref. 56—but is a result of the imaging conditions. Thus, it represents an upper limit for the magnetic point resolution and constitutes the best spatial resolution of stroboscopic Lorentz-microscopy to date.

Due to the high signal-to-noise ratio, the position of the vortex core can be tracked with a precision far below the point resolution, as shown in the following. From the 32 images for every delay t , we form a set of eight identical images, each corresponding to an integration time of 4 min. In a single image, the position of the vortex core is determined by the center of mass of the peak. To visualize the position of the vortex core during one oscillation period, we average over the eight individual measurements (Fig. 2c). An example of their distribution is shown in Fig. 2d. One can clearly see that the points accumulate in an area with a diameter of less than 10 nm . This is significantly smaller than the FWHM of the peak in the image contrast. The deviations from the mean of all position measurements are combined in Fig. 2e. The histogram follows a Gaussian distribution with a standard deviation of $\sigma = 2.0 \text{ nm}$, corresponding to the localization precision of $\pm 2 \text{ nm}$ in each spatial dimension.

Knowledge of the absolute timing of the vortex gyration with respect to the driving current allows us to directly fit our results to the oscillator model presented by Krüger et al.⁵² (see Methods). Although the fitted trajectory agrees well with the data (white and blue lines in Fig. 2b, c), the obtained resonance parameters of the free oscillation frequency $f_0 = 97.9 \pm 2.1 \text{ MHz}$ and the damping

$\Gamma = 74 \pm 13$ MHz indicate a limitation of the description. Specifically, the damping appears unrealistically high, given the resonance curve presented in Methods and previous measurements³². This suggests that additional contributions in the restoring force or the damping may affect the vortex motion, arising, for example, from local disorder^{57–62} or global anharmonicities in the vortex potential (e.g., cubic corrections to the harmonic vortex potential)^{63–66}. In order to obtain direct time-domain information on the damping and possible deviations from a harmonic confinement, we conduct measurements of the free-running relaxation of the vortex in the absence of a driving force.

Damped motion. In the following measurements performed at the same sample, a current at an identical frequency of $f_{\text{ex}} = 101.5$ MHz is applied for a duration of $1 \mu\text{s}$, and is switched off at a zero-crossing of the sine wave at $t = 0$ (see inset of Fig. 3a). Again, the timing was directly determined via small-angle scattering in the vicinity of the permalloy square.

At delay steps of 1 ns, we acquire Lorentz micrographs with an integration time of 3 min. An assembled movie of the data is found in Supplementary Movie 2. The path of the core to its rest position is clearly visible both in the line profiles along the x -axis (Fig. 3a) and in the tracked position of the vortex core (Fig. 3b). A two-dimensional representation of the complete trajectory is given in Fig. 3c. As can be seen from the sense of rotation in Fig. 3c, the vortex polarity is $p = +1$ for this measurement. Thus, we chose a slightly higher current density of $j = 2.9 \times 10^{11} \text{ A m}^{-2}$, which compensates for the smaller orbits in case of an opposite sign between curl and polarity (Eq. (2))⁵².

The trajectory obtained cannot be expressed in terms of a single exponentially decaying sinusoidal function, illustrating systematic deviations from the damped harmonic oscillator model. However, we can extract the momentary frequency and decay rate of the oscillation by fitting an exponentially decaying orbit in a moving window with a size of 20 ns. The blue and green curves in Fig. 3b display the fitted x -component for windows starting at $t_w = 0$ ns and $t_w = 50$ ns, respectively. Good agreement was also obtained for all intermediate values.

The results of the fit are summarized in Fig. 3d, e. The temporal evolution of the orbit diameter D exhibits an approximately linear rather than exponential decay (Fig. 3e). In particular, this can also be seen from the increase of the instantaneous damping Γ , which is plotted as a function of the vortex core velocity v_c in Fig. 3f. The trajectory further experiences a transient rise of the momentary frequency f_0 (Fig. 3d) from 85 to about 92 MHz at medium orbit diameters D . Moreover, allowing for a variable gyration center, we find that the windowed fit reveals a continuous translation of the orbit towards the left (inset of Fig. 3c).

The transient acceleration of the gyratory motion implies the presence of disorder in the vortex potential, and is consistent with time-resolved optical studies^{57,58}. Similarly, the movement of the orbit center suggests a trapping of the vortex core in a pinning site and is further supported by the broadening of the profile in Fig. 3a for delays $t > 80$ ns, likely caused by a stochastic motion at very small diameters. As mentioned above, such frequency shifts have been characterized by other approaches^{16,57,58}. Yet, we have not encountered a real-space measurement of the type of damping observed here. A micromagnetic theoretical study by Min et al.⁶⁰ points towards a possible microscopic origin of the enhanced dissipation. In that work, spatial disorder in the form of variations in the saturation magnetization was found to cause additional damping via deformations of the internal magnetic structure of the vortex. While our observations, in agreement

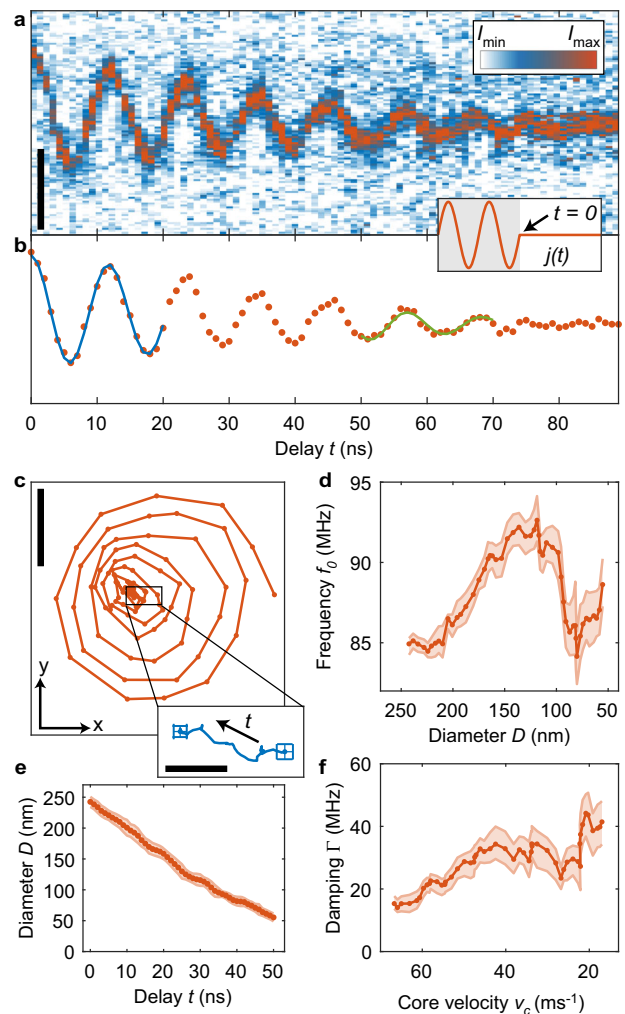


Fig. 3 Damped vortex gyration after switching off the current

($f_{\text{ex}} = 101.5$ MHz, $j = 2.9 \times 10^{11} \text{ A m}^{-2}$). **a** Profiles of the vortex core along the x -axis, illustrating the damped sinusoidal motion towards the equilibrium position (scale bar: 200 nm). **b** Red: Tracked x -position of the vortex core as function of t (scale bar as in (a)). Blue/green: First/last result of the moving-window fit to the vortex trajectory. **c** Spatial vortex core trajectory during the damping. Spacing between the dots is 1 ns (scale bar: 100 nm). (**c**, Inset) Center of the gyration moving over time as determined from the fit (scale bar: 20 nm). **d–f** Fit results of the windowed fit. Shaded regions are one-sigma confidence intervals: **(d)** free oscillation frequency f_0 as a function orbit diameter D . **e** Mean orbit diameter D over delay t . **f** Damping Γ as a function of the vortex core velocity v_c .

with the theoretical calculations, show an increase in f_0 and Γ , particular differences are apparent. Specifically, the damping growth is much more pronounced in our case, such that the ratio Γ/f_0 increases over time, whereas Min et al. have found that it is decreasing⁶⁰. Therefore, our measurements suggest additional contributions to the disorder potential, such as magnetic anisotropy or non-magnetic voids⁶¹. A detailed modeling may be guided by further correlative studies of the structural and chemical composition, facilitated by nanoscale diffraction and spectroscopy available in transmission electron microscopy.

In conclusion, we implemented ultrafast Lorentz microscopy with synchronous RF current excitation and demonstrated its high spatio-temporal resolution by mapping the time-resolved gyration of a magnetic vortex core with an precision of ± 2.0 nm. Future developments will include higher contrast and spatial

resolution from enhanced beam coherence, increased sensitivity from larger duty-cycles and frequencies up to the terahertz range. In combination with more advanced imaging techniques like transport-of-intensity⁵³ based magnetization reconstructions or electron holography^{26–29}, this will enable quantitative imaging of magnetic textures on ultrafast time scales. In our opinion, exposing spin textures, such as vortices and skyrmions, to electrical and electromagnetic stimuli and observing the nanoscopic response will make valuable contributions to fundamental research and device development in ultrafast magnetism. Moreover, the approach can be readily extended to in situ phase contrast imaging in different areas, including electrical switching of multiferroic materials and other correlated systems and heterostructures.

Methods

Instrumentation. The data were acquired at a JEOL 2100F TEM at an acceleration voltage of 120 kV. The microscope is equipped with a Gatan Ultrascan US4000 camera and features an electron gun allowing for a photoemission of electron pulses. Details concerning the electron source have been presented by Feist et al.⁴². Fresnel imaging was performed at a defocus of 520 μm at a low magnification imaging mode, in which the main objective lens is current-free with a small residual field of about 10 mT. The laser system in use is a Ti:Sa regenerative amplifier and seed laser manufactured by Coherent, which outputs 35 fs pulses at a repetition rate of $f_{\text{rep}} = 500$ kHz and a central wavelength of 800 nm. The output of the amplifier is frequency doubled using a β -Barium borate crystal and subsequently stretched to 2.2 ps in a 10 cm SF6 bar before it is focused onto the electron source.

The design of our self-made sample holder is based on that of Pollard et al.³² and consists of a coaxial SMA vacuum feedthrough and a coaxial vacuum cable connected to a coplanar waveguide on a printed circuit board. The laser amplifier system provides an electrical trigger signal which is synchronized to its optical output. This signal is fed into the trigger input of a Keysight 81160A AWG, where it initiates the output of a sinusoidal wave with a fixed number of cycles n_{burst} . For a quasi-continuous excitation of the sample, the burst number and the excitation frequency are set to the same multiple of the repetition rate of the laser amplifier, i.e. $f_{\text{ex}} = n_{\text{burst}} \cdot f_{\text{rep}}$. For non-continuous excitations, there is no constraint on the waveform other than it being shorter than $1/f_{\text{rep}}$.

In quasi-continuous operation special care has been taken to achieve a glitch-and-gap-free output by monitoring the signal with a directional coupler (Mini-Circuits ZFDC-20-4L) and an oscilloscope (Tek DPO71604C with 16 GHz bandwidth). Additionally, we placed a 6dB attenuator after the generator output to suppress standing waves at the RF transmission line, originating from the unmatched sample and a parasitic capacitance of the generator output.

Sample system and reference measurements. The sample consists of a 26 nm thick permalloy ($\text{Ni}_{81}\text{Fe}_{19}$) square of $2.1 \times 2.1 \mu\text{m}^2$ size, which is electrically connected with two gold contacts (100 nm thickness). From a comparison between experimental and simulated Fresnel images, we obtain a saturation magnetization of about $M_S = 600 \text{ kA m}^{-1}$ (see Supplementary Note 1). The substrate is a single crystalline, 35 nm thick silicon membrane with $100 \times 100 \mu\text{m}^2$ windows. The magnetic structure and the contacts were fabricated using electron beam lithography and thermal evaporation. The quality of the lift-off was confirmed using Fresnel imaging, as fabrication errors (e.g., residual magnetic material in the center of the sample) would show up as strong phase objects. A Lorentz micrograph of the unexcited sample recorded with a continuous electron beam is depicted in Fig. 4a. In its equilibrium position, the vortex core is slightly shifted to the right, which is likely caused by a residual out-of-plane field of the current-free objective lens in combination with a small tilt of the sample.

The resonance curve of the vortex oscillator (Fig. 4b) was determined from a Lorentz image series acquired prior to the time-resolved measurement using a continuous electron beam³². A maximum response near $f_{\text{ex}} = 101.5$ MHz is found. Below and above frequencies of 95 MHz and 111 MHz, respectively, the vortex core is pinned and remains stationary.

A comment should be made about possible influences of Joule heating in the time-resolved experiments. The saturation magnetization directly affects the integrated intensity of the vortex feature above the background. From a comparison of the image contrast with and without excitation (Fig. 2a at $t = 0$, and Fig. 4a), this intensity varies by less than ten percent upon current excitation, within the margin of error. We can thus rule out a significant thermal reduction of the saturation magnetization. For the measurements in Fig. 3, despite a higher current density in the five cycles before switching off the current, the average thermal load was lower than in the measurement under continuous excitation. This was achieved by reducing the current amplitude prior to the last five cycles.

Tracking the vortex core. To track the position of the vortex core, we denoised the frames by applying a $3 \times 3 \text{ pixel}^2$ (4.85 nm/pixel) median filter and calculated

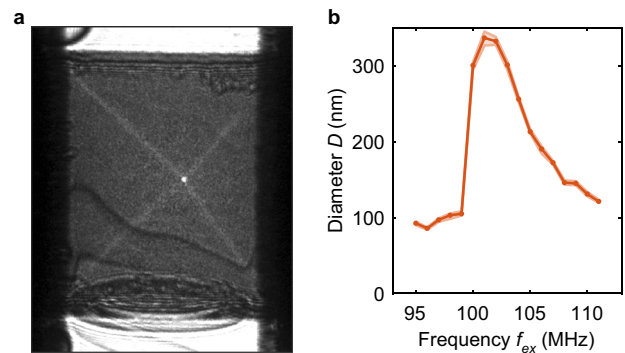


Fig. 4 Preliminary characterization of the sample utilizing an continuous electron beam. **a** Lorentz-micrograph of the unexcited sample system acquired under continuous illumination (scale bar: 1 μm). **b** Orbit-diameter of the vortex gyration as a function of the driving frequency f_{ex} . Shaded regions are one-sigma confidence intervals obtained via bootstrapping the fitting routine.

the center of mass of the pixels of maximum intensity. These pixels were selected via thresholding. The threshold is chosen such that the contributing pixels correspond to a region of about 50 nm in diameter.

Determination of time-zero. We utilize a diffraction mode with long camera length to determine the absolute timing of the current through the nanoisland by measuring the electrical field between the gold contacts³³. Therefore, we form a parallel electron beam close to an edge of an Au electrode in a sufficient distance to the permalloy. This ensures that the electrons are only deflected due to the electric field between the contacts. In diffraction mode, this beam converges to a single point. Choosing a long camera length, we can image a deflection of this spot which is directly proportional to the electric field.

To determine $t = 0$ of the first measurement (continuous sinusoidal excitation), we fit a cosine-function to the delay-dependent position of the electron spot. For the second measurement of the damped motion, we probe delays before and after $t = 0$, which allows us to directly find the last zero-crossing of the sinusoidal current.

Harmonic oscillator model. Passing a current through a non-magnetic/magnetic ($\text{Au}/\text{Ni}_{81}\text{Fe}_{19}$) interface spin polarizes this current due to a difference in the scattering probability between the majority and minority electrons in the conduction band of the magnetic layer⁵. This spin-polarized current exerts a torque on the magnetic domains, altering their configuration and resulting in a displacement of the vortex core. Zhang and Li derived a general micro-magnetic model accounting for adiabatic and nonadiabatic contributions to this spin-transfer-torque (STT) by extending the Landau–Lifshitz–Gilbert (LLG) equation⁶⁷. Based on a generalized Thiele equation^{68,69}, Krüger et al. published a harmonic oscillator model for the movement of a vortex core in a square magnetic thin film, which takes in-plane Oersted fields as well as spin-transfer torques into account. These Oersted fields originate in an inhomogeneous current density inside the magnetic conductor^{47,51,52}. Krüger et al. specify the resulting steady-state trajectory under the influence of a driving current $\mathbf{j}(t) \propto \exp(i\Omega t)\mathbf{e}_x$ and field $\mathbf{H}(t) \propto \exp(i\Omega t)\mathbf{e}_y$, as⁵²

$$\begin{pmatrix} X \\ Y \end{pmatrix} = \text{Re} \left[-\frac{e^{i\Omega t}}{\omega^2 + (i\Omega + \Gamma)^2} \begin{pmatrix} \tilde{j} & \tilde{H}_{\text{cp}} + \frac{D_0}{G_0} |\mathbf{p}\tilde{\xi}| \\ -\tilde{H}_{\text{cp}} - \frac{D_0}{G_0} |\mathbf{p}\tilde{\xi}| & \tilde{j} \end{pmatrix} \begin{pmatrix} \frac{\omega^2}{\omega^2 + \Gamma^2} i\Omega \\ \omega_{\text{p}} + \frac{\omega\Gamma}{\omega^2 + \Gamma^2} i\Omega_{\text{p}} \end{pmatrix} \right] \quad (1)$$

with \tilde{H} and \tilde{j} the normalized magnitudes of the Oersted-field and the spin-polarized current, $\Omega = 2\pi f_{\text{ex}}$ the driving frequency, $\omega = 2\pi f_0$ the free oscillation frequency, Γ the damping constant, and $|D_0/G_0|$ a ratio related to exact magnetic distribution inside the nanoisland. The non-adiabaticity parameter ξ describes the ratio between non-adiabatic and adiabatic contributions in the LLG equation.

The scalar prefactor together with the vector define a trajectory in the form of an ellipse. Due to its symmetry, the matrix in (1) only introduces a rotation and an isotropic dilation to this ellipse. Parameters such as the ellipticity and the phase of the gyration (i.e., the position of the core with respect to the major axis of the ellipse at $t = 0$) are independent of this matrix. Therefore, we can simplify Eq. (1) to

$$\begin{pmatrix} X \\ Y \end{pmatrix} = \text{Re} \left[-\frac{e^{i\Omega t}}{\omega^2 + (i\Omega + \Gamma)^2} A \hat{R}(\theta) \cdot \begin{pmatrix} \frac{\omega^2}{\omega^2 + \Gamma^2} i\Omega \\ \omega_{\text{p}} + \frac{\omega\Gamma}{\omega^2 + \Gamma^2} i\Omega_{\text{p}} \end{pmatrix} \right] \quad (2)$$

with an isotropic dilation A and a rotation of the ellipse by angle θ defined by the

rotation matrix $\hat{R}(\theta)$. From the vector in Eq. (2) it follows directly that the sense of the rotation depends only on the core polarization p , with $p = +1/-1$ resulting in a counter-clockwise/clockwise rotation⁴⁷.

The trajectory in Eq. (2) has five measurable parameters, which equals the number of degrees of freedom of an ellipse (length of the two semiaxes, tilt, frequency) plus an initial phase. This allows us to directly fit the model to our measurement of the continuously driven oscillation by solving the overdetermined system of 42 equations ($X(t)$ and $Y(t)$ for every delay t). As the driving frequency is known, we fix it to $f_{\text{ex}} = 101.5$ MHz. The best fit ($f_0 = 97.9 \pm 2.1$ MHz, $\Gamma = 74 \pm 13$ MHz) is shown as solid line in Fig. 2b (white) and Figs. 2c, d (blue). The errors in the fitted values correspond to 1σ -confidence intervals determined by bootstrapping⁷⁰.

Data availability

The data that support the findings of this study are available from the corresponding author on request.

Received: 12 July 2019; Accepted: 13 December 2019;

Published online: 14 February 2020

References

1. Skyrme, T. A unified field theory of mesons and baryons. *Nucl. Phys.* **31**, 556–569 (1962).
2. Muhlbauer, S. et al. Skyrmion lattice in a chiral magnet. *Science* **323**, 915–919 (2009).
3. Yu, X. Z. et al. Real-space observation of a two-dimensional skyrmion crystal. *Nature* **465**, 901–904 (2010).
4. Hubert, A. & Schäfer, R. *Magnetic Domains*. (Springer, Berlin, Heidelberg, 1998).
5. Ralph, D. & Stiles, M. Spin transfer torques. *J. Magn. Magn. Mater.* **320**, 1190–1216 (2008).
6. Liu, L., Moriyama, T., Ralph, D. C. & Buhrman, R. A. Spin-torque ferromagnetic resonance induced by the spin Hall effect. *Phys. Rev. Lett.* **106**, 036601 (2011).
7. Emori, S., Bauer, U., Ahn, S.-M., Martinez, E. & Beach, G. S. D. Current-driven dynamics of chiral ferromagnetic domain walls. *Nat. Mater.* **12**, 611–616 (2013).
8. Beaupaire, E., Merle, J.-C., Daunois, A. & Bigot, J.-Y. Ultrafast spin dynamics in ferromagnetic nickel. *Phys. Rev. Lett.* **76**, 4250–4253 (1996).
9. Stanciu, C. D. et al. All-optical magnetic recording with circularly polarized light. *Phys. Rev. Lett.* **99**, 047601 (2007).
10. Kampfrath, T. et al. Coherent terahertz control of antiferromagnetic spin waves. *Nat. Photonics* **5**, 31–34 (2011).
11. Eggebrecht, T. et al. Light-induced metastable magnetic texture uncovered by in situ Lorentz microscopy. *Phys. Rev. Lett.* **118**, 097203 (2017).
12. Parkin, S. S. P., Hayashi, M. & Thomas, L. Magnetic domain-wall racetrack memory. *Science* **320**, 190–194 (2008).
13. Fert, A., Cros, V. & Sampaio, J. Skyrmions on the track. *Nat. Nanotechnol.* **8**, 152–156 (2013).
14. Engel, B. et al. A 4-Mb toggle MRAM based on a novel bit and switching method. *IEEE Trans. Magn.* **41**, 132–136 (2005).
15. Mancoff, F. B., Rizzo, N. D., Engel, B. N. & Tehrani, S. Phase-locking in double-point-contact spin-transfer devices. *Nature* **437**, 393–395 (2005).
16. Dussaux, A. et al. Large microwave generation from current-driven magnetic vortex oscillators in magnetic tunnel junctions. *Nat. Commun.* **1**, 8 (2010).
17. Macià, F., Kent, A. D. & Hoppensteadt, F. C. Spin-wave interference patterns created by spin-torque nano-oscillators for memory and computation. *Nanotechnology* **22**, 095301 (2011).
18. Torrejon, J. et al. Neuromorphic computing with nanoscale spintronic oscillators. *Nature* **547**, 428–431 (2017).
19. Krasnyuk, A. et al. Time-resolved photoemission electron microscopy of magnetic field and magnetisation changes. *Appl. Phys. A: Mater. Sci. Process.* **76**, 863–868 (2003).
20. Hiebert, W. K., Stankiewicz, A. & Freeman, M. R. Direct observation of magnetic relaxation in a small permalloy disk by time-resolved scanning Kerr microscopy. *Phys. Rev. Lett.* **79**, 1134–1137 (1997).
21. Fischer, P. Magnetic soft X-ray transmission microscopy. *Curr. Opin. Solid State Mater. Sci.* **7**, 173–179 (2003).
22. von Korff Schmising, C. et al. Imaging ultrafast demagnetization dynamics after a spatially localized optical excitation. *Phys. Rev. Lett.* **112**, 217203 (2014).
23. Kfir, O. et al. Nanoscale magnetic imaging using circularly polarized high-harmonic radiation. *Sci. Adv.* **3**, ea04641 (2017).
24. McVitie, S. et al. Aberration corrected Lorentz scanning transmission electron microscopy. *Ultramicroscopy* **152**, 57–62 (2015).
25. Shibata, N. et al. Atomic resolution electron microscopy in a magnetic field free environment. *Nat. Commun.* **10**, 2308 (2019).
26. Lichte, H. & Lehmann, M. Electron holography-basics and applications. *Rep. Prog. Phys.* **71**, 016102 (2008).
27. Schofield, M., Beleggia, M., Zhu, Y. & Pozzi, G. Characterization of JEOL 2100F Lorentz-TEM for low-magnification electron holography and magnetic imaging. *Ultramicroscopy* **108**, 625–634 (2008).
28. Midgley, P. A. & Dunin-Borkowski, R. E. Electron tomography and holography in materials science. *Nat. Mater.* **8**, 271–280 (2009).
29. Wolf, D. et al. 3D magnetic induction maps of nanoscale materials revealed by electron holographic tomography. *Chem. Mater.* **27**, 6771–6778 (2015).
30. Fu, X. et al. Optical manipulation of magnetic vortices visualized in situ by Lorentz electron microscopy. *Sci. Adv.* **4**, eaat3077 (2018).
31. Berruto, G. et al. Laser-induced Skyrmion writing and erasing in an ultrafast cryo-lorentz transmission electron microscope. *Phys. Rev. Lett.* **120**, 117201 (2018).
32. Pollard, S., Huang, L., Buchanan, K., Arena, D. & Zhu, Y. Direct dynamic imaging of non-adiabatic spin torque effects. *Nat. Commun.* **3**, 1028 (2012).
33. Goncalves, F. J. T. et al. Probing microwave fields and enabling in-situ experiments in a transmission electron microscope. *Sci. Rep.* **7**, 11064 (2017).
34. Vogel, M. *Imaging of Magnetization Dynamics in Temperature Gradients* Phd thesis, University Regensburg (2018).
35. Dömer, H. & Bostanjoglo, O. High-speed transmission electron microscope. *Rev. Sci. Instrum.* **74**, 4369–4372 (2003).
36. Zewail, A. H. Four-Dimensional Electron Microscopy. *Science* **328**, 187–193 (2010).
37. Browning, N. et al. Recent developments in dynamic transmission electron microscopy. *Curr. Opin. Solid State Mater. Sci.* **16**, 23–30 (2012).
38. Bostanjoglo, O. & Rosin, T. Resonance oscillations of magnetic domain walls and Bloch lines observed by stroboscopic electron microscopy. *Phys. Status Solidi (a)* **57**, 561–568 (1980).
39. Park, H. S., Baskin, J. S. & Zewail, A. H. 4D Lorentz electron microscopy imaging: magnetic domain wall nucleation, reversal, and wave velocity. *Nano Lett.* **10**, 3796–3803 (2010).
40. Schliep, K. B., Quarterman, P., Wang, J.-P. & Flannigan, D. J. Picosecond Fresnel transmission electron microscopy. *Appl. Phys. Lett.* **110**, 222404 (2017).
41. Frömter, R. et al. Time-resolved scanning electron microscopy with polarization analysis. *Appl. Phys. Lett.* **108**, 142401 (2016).
42. Feist, A. et al. Ultrafast transmission electron microscopy using a laser-driven field emitter: femtosecond resolution with a high coherence electron beam. *Ultramicroscopy* **176**, 63–73 (2017).
43. Houdellier, F., Caruso, G., Weber, S., Kociak, M. & Arbouet, A. Development of a high brightness ultrafast transmission electron microscope based on a laser-driven cold field emission source. *Ultramicroscopy* **186**, 128–138 (2018).
44. Rubiano da Silva, N. et al. Nanoscale mapping of ultrafast magnetization dynamics with femtosecond Lorentz microscopy. *Phys. Rev. X* **8**, 031052 (2018).
45. Bach, N. et al. Coulomb interactions in high-coherence femtosecond electron pulses from tip emitters. *Struct. Dyn.* **6**, 014301 (2019).
46. Choe, S.-B. Vortex core-driven magnetization dynamics. *Science* **304**, 420–422 (2004).
47. Bolte, M. et al. Time-resolved X-ray microscopy of spin-torque-induced magnetic vortex gyration. *Phys. Rev. Lett.* **100**, 176601 (2008).
48. Bukin, N. et al. Time-resolved imaging of magnetic vortex dynamics using holography with extended reference autocorrelation by linear differential operator. *Sci. Rep.* **6**, 36307 (2016).
49. Bisig, A. et al. Enhanced nonadiabaticity in vortex cores due to the emergent Hall Effect. *Phys. Rev. Lett.* **117**, 277203 (2016).
50. Shinjo, T. Magnetic vortex core observation in circular dots of permalloy. *Science* **289**, 930–932 (2000).
51. Krüger, B. et al. Harmonic oscillator model for current- and field-driven magnetic vortices. *Phys. Rev. B* **76**, 224426 (2007).
52. Krüger, B. et al. Proposal of a robust measurement scheme for the nonadiabatic spin torque using the displacement of magnetic vortices. *Phys. Rev. Lett.* **104**, 077201 (2010).
53. De Graef, M. in *Magnetic Imaging and its Application to Materials. Experimental Methods in the Physical Sciences*, Vol. 36 (eds De Graef, M. & Zhu, Y.) 27–67 (Academic Press, New York, 2001).
54. Zweck, J. Imaging of magnetic and electric fields by electron microscopy. *J. Phys.: Condens. Matter* **28**, 403001 (2016).
55. Schneider, M., Hoffmann, H. & Zweck, J. Lorentz microscopy of circular ferromagnetic permalloy nanodisks. *Appl. Phys. Lett.* **77**, 2909–2911 (2000).
56. Wachowiak, A. et al. Direct observation of internal spin structure of magnetic vortex cores. *Science* **298**, 577–580 (2002).
57. Compton, R. L. & Crowell, P. A. Dynamics of a pinned magnetic vortex. *Phys. Rev. Lett.* **97**, 137202 (2006).

58. Compton, R. L., Chen, T. Y. & Crowell, P. A. Magnetic vortex dynamics in the presence of pinning. *Phys. Rev. B* **81**, 144412 (2010).
59. Min, H., McMichael, R. D., Donahue, M. J., Miltat, J. & Stiles, M. D. Effects of disorder and internal dynamics on vortex wall propagation. *Phys. Rev. Lett.* **104**, 217201 (2010).
60. Min, H., McMichael, R. D., Miltat, J. & Stiles, M. D. Effects of disorder on magnetic vortex gyration. *Phys. Rev. B* **83**, 064411 (2011).
61. Van de Wiele, B., Laurson, L. & Durin, G. Effect of disorder on transverse domain wall dynamics in magnetic nanostrips. *Phys. Rev. B* **86**, 144415 (2012).
62. Leliaert, J. et al. Influence of material defects on current-driven vortex domain wall mobility. *Phys. Rev. B* **89**, 064419 (2014).
63. Guslienko, K. Y., Heredero, L. H. & Chubykalo-Fesenko, O. Nonlinear gyrotropic vortex dynamics in ferromagnetic dots. *Phys. Rev. B* **82**, 014402 (2010).
64. Drews, A. et al. Nonlinear magnetic vortex gyration. *Phys. Rev. B* **85**, 144417 (2012).
65. Stevenson, S. E. et al. Dynamic stabilization of nonequilibrium domain configurations in magnetic squares with high amplitude excitations. *Phys. Rev. B* **87**, 054423 (2013).
66. Guslienko, K. Y., Sukhostavets, O. V. & Berkov, D. V. Nonlinear magnetic vortex dynamics in a circular nanodot excited by spin-polarized current. *Nanoscale Res. Lett.* **9**, 386 (2014).
67. Zhang, S. & Li, Z. Roles of nonequilibrium conduction electrons on the magnetization dynamics of ferromagnets. *Phys. Rev. Lett.* **93**, 127204 (2004).
68. Thiele, A. A. Steady-state motion of magnetic domains. *Phys. Rev. Lett.* **30**, 230–233 (1973).
69. Thiaville, A., Nakatani, Y., Miltat, J. & Suzuki, Y. Micromagnetic understanding of current-driven domain wall motion in patterned nanowires. *Europhys. Lett. (EPL)* **69**, 990–996 (2005).
70. Efron, B. Bootstrap methods: another look at the Jackknife. *Ann. Stat.* **7**, 1–26 (1979).

Acknowledgements

The authors thank Johannes Riebold for his help in designing and testing the in situ TEM Holder. Furthermore, we acknowledge useful discussions with Mathias Kläui, Henning Ulrichs and Michael Vogel and assistance from the Göttingen UTEM Team, especially Armin Feist, Nara Rubiano da Silva, Nora Bach, Thomas Danz and Karin Ahlborn. This work was funded by the Deutsche Forschungsgemeinschaft (DFG) in the Collaborative Research Center “Atomic Scale Control of Energy Conversion” (DFG-SFB 1073, project

A05) and via resources from the Gottfried Wilhelm Leibniz-Price. We gratefully acknowledge support by the Lower Saxony Ministry of Science and Culture and funding of the instrumentation by the DFG and VolkswagenStiftung.

Author contributions

C.R., S.S., and M.M. conceived the project. M.M. prepared the sample. M.M. conducted the experiment with help from J.H.G. M.M. and J.H.G. evaluated the data and discussed the results with all authors. M.M. and C.R. wrote the paper with inputs from all authors.

Competing interests

The authors declare no competing interests.

Additional information

Supplementary information is available for this paper at <https://doi.org/10.1038/s42005-020-0301-y>.

Correspondence and requests for materials should be addressed to C.R.

Reprints and permission information is available at <http://www.nature.com/reprints>

Publisher’s note Springer Nature remains neutral with regard to jurisdictional claims in published maps and institutional affiliations.



Open Access This article is licensed under a Creative Commons Attribution 4.0 International License, which permits use, sharing, adaptation, distribution and reproduction in any medium or format, as long as you give appropriate credit to the original author(s) and the source, provide a link to the Creative Commons license, and indicate if changes were made. The images or other third party material in this article are included in the article’s Creative Commons license, unless indicated otherwise in a credit line to the material. If material is not included in the article’s Creative Commons license and your intended use is not permitted by statutory regulation or exceeds the permitted use, you will need to obtain permission directly from the copyright holder. To view a copy of this license, visit <http://creativecommons.org/licenses/by/4.0/>.

© The Author(s) 2020